4-1-2021

Seismic Performance of RC Beam-Column Edge Joints Reinforced with Austenite Stainless Steel

C Xu

Moncef L. Nehdi
Western University

Maged A. Youssef
Western University, youssef@uwo.ca

L. V. Zhang

Seismic Performance of Concrete Frame Edge Joints Reinforced with Austenite Stainless Steel

Chunyi XU,[1,2], Moncef L. NEHDI*[1], Maged YOUSSEF[1], Tao WANG[2], Lei ZHANG[2]

[1.] *Department of Civil and Environmental Engineering; Western University, London, Ontario, Canada, N6A 5B9.*
[2.] *School of Civil Engineering; Shenyang Jianzhu University, Shenyang, Liaoning, China, 110168.*

ABSTRACT

Using stainless steel (SS) reinforcement can mitigate colossal damage inflicted to reinforced concrete (RC) structures worldwide due to corrosion. However, there is still dearth of studies on the seismic behavior of SS-RC structures. Hence, an experimental investigation was conducted to explore the seismic performance of SS-RC frame edge joints. Ordinary steel and SS rebar RC frame edge joints exhibited similar bending-shear failure patterns at the root of the beam. The load bearing capacity of SS-RC frame edge joint specimens was greater than that of control ordinary steel RC counterparts. The yield and ultimate displacements of the SS-RC specimens were both larger, while the displacement ductility coefficient was smaller than that of control ordinary specimens, respectively. Generally, SS-RC specimens met design code ductility requirements under earthquake loading, with adequate plastic deformation ability. A constitutive relationship for SS rebar was proposed in this study and used to conduct finite element simulation of the tested specimens. Good correlation between simulation and experimental results was observed. Thus, a parametric study was conducted to numerically study the effects of the axial compression, longitudinal and hoop reinforcement ratios on the seismic behavior of SS-RC joints. The findings could provide a theoretical basis for design provisions of SS reinforced concrete structures.

Keywords: Stainless steel; Reinforced concrete; Frame; Beam-column joint; Seismic; Experiment; Numerical simulation.

Corresponding author: Tel: (519) 661-2111 x88308; Email: mnehdi@uwo.ca

1. Introduction

Corrosion of steel has been, by far, the costliest damage mechanism in reinforced concrete (RC) structures, compromising the structural integrity and safety of a large portfolio of buildings, bridges, tunnels, lifeline systems and other critical civil infrastructure around the world. While associated with higher materials cost, stainless steel (SS) can prevent corrosion, and thus can be cost competitive based on life cycle analysis. Yet, research on SS-RC structures has so far focused primarily on its rust resistance and on the mechanical performance of individual members, such as beams and columns. There is dearth of research on the seismic performance of concrete structures reinforced with SS, which has hindered wider implementation of SS rebar in large-scale construction.

Substantial research has demonstrated that beam-column joints (BCJs) are paramount in the earthquake behavior of RC frame structures. For instance, Youssef and Ghobarah [1] proposed models for the shear, bond slip, and flexural deformations in the plastic hinge regions of BCJs. Sadjadi [2] carried out an experimental study on 7 beam-column edge joints and showed that when more stirrups were arranged in the core area of the joints, the BCJs had better shear bearing capacity after yielding and full bending capacity of the beam could be mobilized. Ghobarah and El-Amoury [3] reported on 12 full-scale RC edge joint tests to show that the BCJ flexural strength ratio played a very important role in determining the position of the plastic hinge.

The role of stirrups in the core area of BCJs is mainly to bear shear forces and restrain concrete deformation in the core area. Meas *et al*. [4] presented experimental results of 4 lightly reinforced concrete exterior BCJs with and without beam stubs under cyclic loading. The strut-and-tie model based on the recorded strain in the joint transverse reinforcement was used to determine the force flow in the joint core. Ding *et al.* [5] tested 7 full-scale joints to investigate the seismic performance of BCJs with design for deconstruction (DfD) connections. The proposed concrete frame joint with DfD connections had favorable seismic performance, though with smaller displacement ductility. Such experimental studies and theoretical analyses on the seismic performance of ordinary BCJs have laid a solid foundation for the seismic design of BCJs with conventional steel rebar reinforcement.

Conversely, research on stainless steel reinforced concrete structures is still in its infancy. Existing studies [e.g. 6,7,8] compared the corrosion resistance of SS-RC and ordinary RC specimens, showing that SS rebar had superior rust resistance. This has led to several applications of SS, particularly in offshore RC structures. Other studies have explored the design and behavior of SS tube concrete structural members. For instance, Uy *et al.* [9] studied the behavior of short and slender concrete-filled SS tubular columns. Ellobody and Young [10] studied the design and behavior of concrete-filled cold-formed SS tube columns. Ye *et al.* [11] investigated the mechanical behavior of concentrically and eccentrically loaded concrete-filled SS tube tensile members. The concrete infill effectively worked with the outer SS tube. All tensile members showed ductile behavior, yet the SS tube concrete was considered costly.

There is limited research on the mechanical properties of SS bars in concrete members. Ertzibengoa *et al.* [12] investigated the bond behavior of stainless steel rebars on RC specimens. A bond stress–slip relationship for SS bars was established. This research showed that the bond behavior of SS rebars was comparable to that of carbon steel bars. Pauletta, *et al.* [13] and Xu, *et al.* [14] conducted testing on the bond between SS rebar and concrete. They reported that SS rebar had good bonding properties with concrete, and formulas for calculating the bonding force between SS rebar and concrete were proposed. Li *et al.* [15] compared the flexural and shear capacity of SS-RC beams with that of ordinary RC beams and showed that the ultimate shear force of SS-RC beams was significantly higher than that of control ordinary RC beams. Zhang *et al.* [16] experimentally studied the bending performance of concrete beams reinforced with SS and ordinary steel bars. The load capacity of SS-RC beams was higher than that of ordinary steel bar counterparts. Huang [17] conducted fatigue load tests on SS-RC beams and ordinary RC beams to study the crack development and width, number of stress cycles, and stress-strain relationship between steel and concrete. Test results showed that the cumulative damage of concrete and steel bars in SS-RC beam specimens was smaller than that in ordinary RC beam counterparts. Zhang [18] investigated the mechanical properties of SS-RC slabs through static fatigue tests. Test results showed that the fatigue life of SS bar concrete slabs was 1.1 times that of control ordinary RC slabs.

The Hong Kong-Zhuhai-Macao Bridge connecting Hong Kong, Macau and Zhuhai is currently the longest sea-crossing bridge in the world. This bridge used nearly 3,500 tons of SS bars including duplex SS bars for the cap, tower and pier. Experimental SS bars and normal bars used in the present study are from the same manufacturer of SS bars used in the construction of the Hong Kong-Zhuhai-Macao Bridge. Compared with ordinary carbon steel and low alloy steel, the advantages of SS bar include: i) superior corrosion resistance and durability; ii) reduced requirements for protective layer of concrete; iii) good processability, impact resistance and ductility; iv) good adaptability in both high and low temperature environments; v) anti-magnetic penetration and anti-radiation performance; vi) recyclability; and vii) reduced total life cycle costs. The current body of knowledge discussed above indicates that SS rebar has adequate performance and can be applied in RC structures. However, little research on the seismic behavior of SS-RC structures exists, especially for BCJs. This lack of research and need for pertinent design provisions have hindered large-scale application of SS-RC. Accordingly, the present study examines the seismic performance SS-RC BCJs and develops predictive numerical tools for its behavior.

2. Experimental Program

2.1 Test Specimens

Four half-scale beam-column edge joints were designed as per design code provisions [19]. Joints BJD-1, BJD-2, and BJD-3 were reinforced with SS bars with a strength grade of 500, while the contrastive joint BJD-4 was reinforced with HRB400E ordinary steel bar (HRB400E refers to ordinary hot rolled ribbed reinforcement with yield strength of 400 MPa). The suffix E indicates seismic performance of the rebar with load capacity between yield and tensile strength of 25% of yield strength, and maximum elongation of 9%, as opposed to 7.5% for ordinary rebar. This ensures better ductility under earthquake force. The used concrete mixture had 28-d compressive strength of 49.8 MPa. Details of the joint are shown in **Fig. 1**. **Table 1** provides further information about the main test parameters: hoop ratio, column axial load ratio, and column longitudinal ratio.

2.2 Test Setup

Figure 2 shows a schematic of the test setup. Digitally controlled MTS machine was used to apply quasi-static load on the free end of the beam. The upper and lower ends of the column were hinged. The lower end of the column was connected with the spherical hinge anchored on the ground. The upper end of the column was instrumented with a pressure sensor. The horizontal tie rod and oil pressure jack on top of the column were connected through a spherical hinge. The other end of the horizontal tie rod was connected with the rigid wall through a hinged support, so as to ensure that the upper end of the column does not undergo horizontal displacement.

The main measurements were the vertical loads and displacements at the ends of beams and column, shear deformation of the joint, longitudinal steel strain of the beam and column in the plastic hinge region, and stirrup strain in the core region of the joint. The specific measuring devices include two force sensors set at the top of the column and the end of the beam; LVDTs at the column end, beam end, beam plastic hinge section, column plastic hinge section and the joint core area. The LVDTs in the joint core area were cross; A total of 8 LVDTs were installed as shown in **Fig. 3**. Strain gauges were also attached on select stirrups and longitudinal bars in the joint core area and the plastic hinge area of beam and column to measure strain development in reinforcing bars (**Fig. 4**).

The test started by applying constant axial force on top of the column (the test axial pressure ratio was 0.3). The cyclic load was increased at the free end of the beam in increments of 5 kN in each step until yielding behavior was observed. The test was then changed to displacement control by applying displacements of ±2Δy, ±3Δy, where Δy is the yield displacement. Each load cycle was repeated twice. The test was stopped when the load dropped by 15% or more, and the joint was then considered at a failure stage.

2.3 Experimental Behavior

Generally, joints behaved in a similar manner. The longitudinal rebars of the beam reached the yield strength, then a plastic hinge was formed at the root of the beam. For joint BJD-1, at the initial stage of loading, the beam behaved in an elastic manner. At the load of 20 kN, a vertical crack appeared in the beam near the joint, having a width of about 0.12 mm, as shown in **Fig. 5(a).** Then longitudinal rebars of the beam reached the yield strength and diagonal cracks were observed in the joint area at a load of about 38 kN (**Fig. 5(b)**). The corresponding yield displacement was 19 mm. With the increase of displacement load, cracks became wider and more abundant. Additional vertical cracks formed in the beam, while diagonal cracks in the joint could also be observed as shown in **Fig. 5(c)**. At a displacement of $5\Delta_y$, the load decreased to 28 kN, which is less than 85% of the ultimate bearing capacity, which represents failure, with the joint damage shown in **Fig. 5(d)**.

The longitudinal reinforcement ratio of the column of specimen BJD-2 was lower than that of BJD-1. During the failure process, BJD-2 had more cracks in the joint core area than BJD-1, which tended to extend to both ends of the column. Moreover, on the specimen side without beam restraint, the concrete in the core area exhibited cracks, as shown in **Fig. 6**. The stirrup ratio of the joint core area of BJD-3 was lower than that of BJD-1. Thus, BJD-3 displayed more damage in the joint core area during the failure process. Moreover, on its side without beam restraint, concrete in the core area incurred external bulge, as shown in **Fig. 7**.

The reinforcement ratios of specimens BJD-4 and BJD-1 were similar, yet the type of steel bar was different. Because the joint was designed according to the strong column and weak beam concept, the strength of BJD-4 reinforcement was lower than that of BJD-1. In the process of specimen failure, the bearing load was minimum, that is, the bending moment transferred to the column was minimum. When the strength of the column and core area of the joint had not yet been fully mobilized, the root of the beam was damaged, while there was no crack in the core area of the joint, (**Fig. 8)**. When the load reached 12 kN, a crack in the longitudinal direction appeared at the upper part of the beam root near the joint core area, with a width of about 0.09 mm. When the tensile reinforcement of the beam reached the yield strain, it was considered that the specimen had reached its yield state. At this stage, the crack at the root of the beam continued to expand, and the load reached 24.6 kN, which was recorded as the yield load P_y, while the displacement at the loading point was recorded as the yield displacement Δ_y = 12.5 mm, which was taken as the first loading cycle of displacement control. The test was then transferred to the displacement control stage. When the load reached $7\Delta_y$, the bearing capacity of the test specimen rapidly dropped to 17 kN, reaching below 85% of the ultimate capacity. At this stage, the concrete in the compression zone at the root of the beam of the joint was severely crushed, which was consider.

Considering strain gauge data, it was found that when the specimens were damaged, the longitudinal reinforcement of the beam in each specimen reached the yield strain value, while the longitudinal reinforcement of the column and stirrup in the joint core area had not reached the yield strain value, which is consistent with the failure mode of the test.

2.4 Load

The loads causing cracking, yielding and failure for specimens BJD-1, BJD-2, BJD-3 and BJD-4 are shown in **Table 2**. The yield load and ultimate load of specimens BJD-1, BJD-2, BJD-3 were comparable. If failure of the beam occurred before that of the joint, and the beam reinforcements were similar, the reinforcement of the column and stirrup in the joint core area had no clear effect on the yield load and ultimate bearing capacity of the joint. The three specimens had little difference in cracking load, yield load and ultimate load, which is likely caused by minor differences in the placement of steel bars in the process of specimen fabrication. Compared with specimen BJD-4, the cracking load of BJD-1 increased by 66.7%, while the yield load increased by 54.5%, and the ultimate load increased by 22.3%. The strength grade of SS bars was 500, while that of carbon steel bars was 400. Thus, the bearing capacity of the former was stronger in each load stage.

2.5 Hysteresis and Skeleton Curves

Figure 9 compares hysteresis curves of specimens BJD-1~BJD-3 to that of BJD-4. Both joint specimens with SS and HRB400E bars displayed curves with relatively full bow shape, and the pinching phenomenon was not observed. The yield and ultimate displacements of specimen BJD-4 were smaller, but its hysteresis loop was fuller in the yield stage. The development trend of the hysteretic curves for BJD-1~BJD-3 was basically similar, and hysteretic loops were relatively full. This indicates that the SS joints had excellent plastic deformation and energy dissipation capacity. At the initial stage, the load-displacement curve was linear, with little residual deformation in the unloading process. Before yielding, the hysteretic curve showed a stable bow shape, while in the unloading process, the residual deformation and stiffness degradation were small. After yielding, the stiffness of the specimen displayed a degenerate trend, and the bearing capacity also tended to decrease. As the load increased, the deformation of the joint core increased. Compared with the initial loading period, the deformation rate also increased significantly. At this point, the curve had obvious residual deformation and pinched behavior.

The comparison of skeleton curves is shown in **Fig. 10**. The shapes of curves for the four specimens were comparable, which shows that the energy dissipation capacity of the SS-RC specimens was similar to that of the control BJD-4 specimen. The yield and ultimate loads of BJD-4 were smaller, while the corresponding characteristic displacement was comparable to that of SS-RC specimens. When the root of the beam was damaged first, increasing the longitudinal reinforcement ratio of the column and stirrup ratio of the joint core area did not change significantly the yield load, ultimate load and corresponding characteristic displacement.

2.6 Ductility

According to the ratio of the ultimate displacement Δ_u and yield displacement Δ_y of the specimen, the displacement ductility coefficient of the specimen is expressed as [20]:

$$\mu = \frac{\Delta_\mu}{\Delta_y} \quad (1)$$

Where: μ = Ductility coefficient; Δ_μ= Ultimate displacement (mm); Δ_y= Yield displacement (mm). Displacement ductility coefficients are listed in **Table 3**. For SS reinforced BCJs, the displacement ductility coefficients (for BJD-1, BJD-2 and BJD-3) were comparable. The yield and ultimate displacements of the three SS RC BCJ specimens were both larger, but the displacement ductility coefficient was smaller than that of the BJD-4 specimen. This is because BJD-4 used HRB400E, which is hot-rolled ribbed steel bars with excellent seismic performance. The essential difference between BJD-4 and ordinary carbon steel reinforcement BCJ specimens was that the maximum elongation of ordinary steel bars was increased from 7.5% to 9%.

The required displacement ductility coefficient of RC seismic structures is usually 3~4 [19]. It can be observed in **Table 3** that the ductility coefficient μ of each specimen was between 5.62~6.63, which meets the ductility requirements for RC structures under earthquake action, indicating that the ductility of each specimen was adequate. Therefore, RC structural members with stainless steel bar could also achieve adequate plastic deformation capacity under earthquake action.

2.7 Energy Dissipation

Using the calculation method given in the "Code for Building Seismic Test Methods (JGJ 101-96)"[20], the energy dissipation coefficient E and the equivalent viscous damping coefficient h_e were obtained in order to quantitatively analyze the energy dissipation capacity of the test specimens at the cracking, yield and ultimate stages. **Table 4** lists the energy dissipation coefficients and the equivalent viscous damping coefficients for the test specimens.

The energy dissipation of BJD-1, BJD-2 and BJD-3 was comparable in each stage, which shows that when the beam reinforcements were similar and the beam bars incurred yielding prior to that of the joint, increasing the longitudinal reinforcement ratio of the column and the stirrup ratio of the joint core area did not significantly increase the energy dissipation of the joint. The energy dissipation coefficient and equivalent viscous damping coefficient of BJD-1, BJD-2 and BJD-3 were higher than that of BJD-4 in both the cracking and yield stages, but were lower in the ultimate stage, which indicates that HRB400E reinforcement had better energy reserve capacity under seismic action.

3. Finite Element Model

3.1 Concrete

The uniaxial stress-strain curve of concrete according to the GB50010-2010) [19] code for design of concrete structures was adopted in developing the finite element model (**Fig. 11**). The stress-strain curve of uniaxial tension of concrete can be determined via the following formula:

$$\sigma = (1 - d_t)E_C\varepsilon \tag{2}$$

$$d_t = \begin{cases} 1 - \rho_t[1.2 - 0.2x^5] & (x \le 1) \\ 1 - \frac{\rho_t}{\alpha_t(x-1)^{1.7}+x} & (x > 1) \end{cases} \tag{3}$$

$$x = \frac{\varepsilon}{\varepsilon_{t,r}}\ ,\ \ \rho_t = \frac{f_{t,r}}{E_c\varepsilon_{t,r}}$$

Where: α_t = parameter value of the descending phase of the uniaxial tensile stress-strain curve of concrete; $f_{t,r}$ = representative value of concrete uniaxial tensile strength that can be taken as f_t, f_{tk}, f_{tm} as required; $\varepsilon_{t,r}$ = peak tensile strain of concrete corresponding to the representative value of uniaxial tensile strength $f_{t,r}$; and d_t = damage evolution parameter of concrete under uniaxial tension.

The stress-strain curve for uniaxial compression of concrete can be expressed as:

$$\sigma = (1 - d_c)E_c\varepsilon \tag{4}$$

$$d_c = \begin{cases} 1 - \frac{\rho_c n}{n-1+x^n} & (x \leq 1) \\ 1 - \frac{\rho_c}{\alpha_c(x-1)^2+x} & (x > 1) \end{cases} \tag{5}$$

$$\rho_c = \frac{f_{c,r}}{E_c\varepsilon_{c,r}}, \quad n = \frac{E_c\varepsilon_{c,r}}{E_c\varepsilon_{c,r} - f_{c,r}}, \quad x = \frac{\varepsilon}{\varepsilon_{c,r}}$$

Where: α_c = parameter value of the descending phase of the uniaxial compression stress-strain curve of concrete; $f_{c,r}$ = representative value of concrete uniaxial compression strength, which can be taken as f'_c, f_{ck}, f_{cm} as required; $\varepsilon_{t,r}$ = peak compression strain of concrete corresponding to the representative value of uniaxial compression strength f_{cr}; and d_c = damage evolution parameter of concrete under uniaxial compression. The mechanical properties of concrete are shown in **Table 5**.

3.2 Steel Rebar

Tensile load and modulus of elasticity tests were carried out on both the SS and ordinary bars with diameter of 6 mm, 16 mm and 20 mm. The reported results are average values obtained on three identical specimens. The yield strength, tensile strength and modulus of elasticity of the steel bars were measured in accordance with the requirements of GB/T228-2002 [21] "Tensile Test Method for Metallic Materials at Room Temperature". In order to measure the elastic modulus of SS, each bar was instrumented with a strain gauge, and data was collected by a data acquisition system, as shown in **Fig. 12.** The measured material parameters are reported in **Table 6**.

The experimentally measured stress-strain curves for SS were adopted, along with the double-diagonal model, as shown in **Fig. 13**. The yield load f_y, ultimate load $f_{s,u}$, ultimate strain ε_s, elastic modulus E_S and other parameters of the steel bar model were all measured experimentally. The stress-strain relationship was calculated as follows:

When $\varepsilon_s \leq \varepsilon_y$, take $\sigma_s = E_s\varepsilon_s$ (6)

When $\varepsilon_y \leq \varepsilon_s \leq \varepsilon_s$, take $\sigma_s = f_y + (\varepsilon_s - \varepsilon_y)\tan\theta''$ (7)

Where: $\tan\theta'' = E_s'' = \frac{f_{s,u} - f_y}{\varepsilon_{s,u} - \varepsilon_y}$ (8)

4. Model Validation

4.1 Failure Modes

Failure modes of test specimens and equivalent simulated finite element analysis are shown in **Fig. 14.** The simulation results had behavior in agreement with test results. The longitudinal reinforcement of the beam yielded first. It could be observed that the concrete at the end of the beam was crushed. All specimens were damaged due to failure of the plastic hinge at the end of the beam.

4.2 Hysteretic Curves

Figure 9 compares hysteresis curves from experimental tests to that of the numerical simulation. The hysteresis curves from finite element analysis were in good agreement with the corresponding experimental hysteresis curves. The calculated data error was less than 18%. The simulated mode of failure was similar to that observed experimentally. This indicates that the modeling method, assumed boundary conditions and overall finite element simulation were reasonable. Thus, the model could be further used to carry out parametric analyses.

5. Parametric Analyses

Finite element model simulations were conducted for the reinforced concrete beam-column edge joints reinforced with SS and normal steel rebar under quasi-static loading. The parameters considered in the parametric study included the axial compression ratio, longitudinal reinforcement ratio and hoop ratio, as shown in **Table 7**.

5.1 Axial Compression Ratio

Figure 15 illustrates the effect of the axial compression ratio of the column on the beam load versus beam end displacement curves. It can be observed that the axial compression ratio had a significant influence on the shear capacity of the joint. In a certain range, the increase of axial compression effectively improved the shear strength of the joint. However, when the axial compression ratio exceeded a certain threshold limit (i.e. axial pressure was too large), premature crushing of the concrete in the joint core area occurred, which decreased the shear strength and the ductility of joint.

5.2 Effect of Longitudinal Reinforcement Ratio of Column

Figure 16 depicts the effect of the longitudinal reinforcement ratio of the column on the beam load versus beam end displacement curves. It can be observed that if the reinforcement ratio of the longitudinal tensile steel bar of the column was increased, the deformation capacity of the cross-section of the column was enhanced after the longitudinal reinforcement of the column reached the yield strength. This trend increased linearly with increasing ratio of longitudinal reinforcement. Under the condition of no yield failure at the root of the beam, the ultimate bearing capacity of the joints could be effectively improved by increasing the ratio of longitudinal reinforcement of the column. Specimens BJD-1 and BJD1-04 satisfied the design requirements of "strong column weak beam" concept. In the case of yield failure at the root of the beam, simply increasing the ratio of the longitudinal reinforcement of the column hardly affected the bearing capacity of the joints.

5.3 Effect of Hoop Reinforcement Ratio in Joint Core Area

Figure 17 illustrates the influence of the hoop reinforcement ratio of the joint core area. It can be observed that the ultimate bearing capacity of the joints could be effectively improved by increasing the hoop ratio of the joint core area without yielding at the root of the beams. If yielding occurred at the root of the beam and only the hoop ratio in the core area was increased, the shear capacity was not significantly changed.

6. Conclusions

This study experimentally investigated the seismic behavior of reinforced concrete beam-column edge joint specimens reinforced either with stainless steel rebar versus conventional steel rebar. A finite element model was developed, and a parametric study was carried out to capture the influence of key design parameters on the overall BCJ behavior. The following conclusions can be drawn:

- The failure patterns of RC BCJ specimens made with either SS or ordinary steel rebar were found to be similar, both exhibiting bending-shear failure at the root of the beam.
- The load bearing capacity of BCJ specimens reinforced with SS rebar was greater at all loading stages than that of corresponding control specimens reinforced with normal rebar.
- The yield and ultimate displacements of the BCJ specimens reinforced with SS rebar were both larger than that of control counterparts reinforced with ordinary rebar, but the

displacement ductility coefficient was smaller than that of the control ordinary specimens.

- The ductility coefficient μ of the test specimens was between 5.62 and 6.63, which exceeds the requirements of ductility for RC structures under earthquake action.
- When the axial compression ratio exceeded a certain threshold value, concrete in the core area of BCJs would be prematurely crushed, which decreased ductility of the BCJ specimens.
- When the "strong column and weak beam" concept was satisfied, the shear bearing capacity of BCJs would be improved by increasing the longitudinal reinforcement ratio of the column.
- If the beam did not incur yielding, increasing the hoop ratio of the core area could effectively enhance the shear capacity of joints.
- Overall, the results indicate that stainless steel rebar satisfies seismic design requirements. Considering its durability benefits, it could make it cost competitive on a life cycle analysis basis and a strong contender to replace conventional rebar in offshore reinforced concrete structures and those located in highly corrosive environments.

Acknowledgements

This project was supported by the National Natural Science Foundation of China (51408373), The Educational Department of Liaoning Province Project (lnfw201905), and Foundation of Basic Discipline of Shenyang Jianzhu University (CXPY2017022).

References

[1] Youssef, M; Ghobarah, A., "Modelling of beam-column joints and structural walls", *Journal of Earthquake Engineering*, 2001, Vol. 5, No. 1, pp. 93-111.

[2] Sadjadi, R., "Analytical modeling of the shear behavior of reinforced concrete exterior beam-column joints", *Master's Thesis, Ryerson University*, 2003, 189 p.

[3] Ghobarah, A; El-Amoury, T., "Seismic rehabilitation of deficient exterior concrete frame joints", *Journal of Composites for Construction*, 2005, Vol. 9, No. 5, pp. 408-416.

[4] Meas, K; Li, B; Imran, I., "Seismic performance of lightly reinforced concrete exterior beam-column joints", *Advances in Structural Engineering*, 2012, Vol. 15, No. 10, pp. 1653–1672.

[5] Ding, T; Xiao, J; Chen, E; Khan, A., "Experimental study of the seismic performance of concrete beam-column frame joints with DfD connections", *Journal of Structural Engineering*, 2020, Vol. 146, No. 4, pp. 1-16.

[6] García-Alonso, M.C.; Escudero, M.L.; Mirandaa, J.M.; Vega, M.I.; Capilla, F.; Correia, M.J.; Salta, M.; Bennani, A.; Gonzáleza; J.A., "Corrosion behaviour of new stainless steels reinforcing bars embedded in concrete", *Cement and Concrete Research*, 2007, Vol. 37, No. 10, pp. 1463-1471.

[7] Dimitri, V; ValaMark, G; Stewartb., "Life-cycle cost analysis of reinforced concrete structures in marine environments", *Structural Safety*， 2003, Vol. 25, No. 4, pp. 343-362.

[8] Markeset, G; Rostam, S; Klinghoffer, O., "Guide for the use of stainless steel reinforcement in concrete

structures", *Norwegian Building Research Institute*, 2006, part 7, pp. 47-53.

[9] Uy, B; Zhong,T; Han, L., "Behaviour of short and slender concrete-filled stainless steel tubular columns", *Journal of Constructional Steel Research*, 2011, Vol. 67, No. 3, pp. 360-378.

[10] Ellobody, E. and Young, B., "Design and behaviour of concrete-filled cold-formed stainless steel tube columns", *Engineering Structures*, 2006, Vol. 28, No. 5, pp. 716-728.

[11] Ye, Y; Li, W; Guo, Z., "Performance of concrete-filled stainless steel tubes subjected to tension: Experimental investigation", *Thin-Walled Structures*, 2020, Vol. 148, No. 3, pp. 1-15.

[12] Ertzibengoa, D; Matthys, S; Taerwe, L., "Bond behaviour of flat stainless steel rebars in concrete", *Materials and structures*, 2012, Vol 45, No. 11, pp. 1639-1653.

[13] Pauletta, M; Rovere, N; Randl, N; Russo, G., "Bond-Slip Behavior between Stainless Steel Rebars and Concrete", *Materials*, 2020, Vol 13, No.4, pp. 1-17.

[14] Xu, C; Yuan, Y; Lu, B., "Experience and finite element analysis of bond behavior between austenitic stainless steel bars and concrete", *Concrete*, 2020, No. 2, pp. 61-66.

[15] Li, C; Geng, H; Li, Q., "Experimental study of stainless steel reinforced concrete beams", *Journal of Highway & Transportation Research & Development*, 2017, Vol. 13, No. 1, pp. 15-18.

[16] Zhang, G; Xu,Y; Ding, Z., "Experimental study on the bending performance of stainless steel reinforced concrete beams", *Railway Construction*, 2010, Vol. 31, No. 5, pp. 35-40.

[17] Huang, J., "Experimental study on fatigue performance of stainless steel reinforced concrete bridge beams." *Master's Thesis, Guangdong University of Technology*, 2013.

[18] Zhang, Y., "Experimental research on fatigue performance of stainless steel reinforced concrete slabs." *Master's thesis, Guangdong University of Technology*, 2014.

[19] GB 50010-2010., "Code for design of concrete structures", *China Building Industry Press*, Beijing, 2010.

[20] JGJ 101-96., "Code for building seismic test methods", *China Building Industry Press*,Beijing, 1997.

[21] GB/T 228.1-2010., "Tensile test method for metallic materials at room temperature", *China Building Industry Press*, Beijing, 2010.

Table 1. Details of tested joints

Joint Number	Beam Longitudinal Bars	Beam Hoop Ratio/%	Column Longitudinal Bars	Column Hoop Ratio/%	Joint Hoop Ratio/%	Column Axial Compression Ratio
BJD-1	4S16	0.337	6S20	0.226	0.5652	0.3
BJD-2	4S16	0.337	6S16	0.226	0.5652	0.3
BJD-3	4S16	0.337	6S20	0.226	0.2830	0.3
BJD-4	4H16	0.337	6H20	0.226	0.5652	0.3

S: Stainless steel bar S30408; H: Carbon steel bar HRB400E.

Table 2. Characteristic loads for the tested joints

Joint number	Cracking load(kN)	Yield load(kN)	Ultimate load (kN)
BJD-1	20	38	45
BJD-2	16	35	50
BJD-3	17	37	43
BJD-4	12	25	37

Table 3. Displacement ductility coefficient

Joint number	Yield displacement Δ_y/mm		Ultimate displacement Δ_u/mm		Displacement ductility coefficient μ		
	Positive	Reverse	Positive	Reverse	Positive	Reverse	Mean Value
BJD-1	19.0	-18.5	106.0	-104.5	5.58	5.65	5.62
BJD-2	18.0	-18.0	105.2	-100.4	5.84	5.58	5.71
BJD-3	18.0	-18.5	104.5	-101.5	5.81	5.49	5.65
BJD-4	12.5	-13.5	86.5	-85.5	6.92	6.33	6.63

Table 4 The energy dissipation coefficient and the equivalent viscous damping coefficients

Joint number	Cracking stage		Yield stage		Ultimate stage	
	E	h_e	E	h_e	E	h_e
BJD-1	0.47	7.48%	0.55	8.76%	1.43	22.77%
BJD-2	0.44	7.01%	0.53	8.44%	1.44	22.92%
BJD-3	0.48	7.64%	0.54	8.59%	1.42	22.61%
BJD-4	0.42	6.69%	0.47	7.48%	1.72	27.38%

Table 5. Concrete mechanic performance

Concrete strength grade	Elasticity modulus（N/mm²）	Poisson's ratio	Density（kg/m³）	Measured value of compressive strength（MPa）	Measured value of tensile strength（MPa）
C40	32500	0.2	2400	49.8	4.98

Table 6. The result of steel mechanical property test

Steel types	Diameter of steel bar d (mm)	Yield strength σy（N/mm²）	Tensile strength σu（N/mm²）	Yield strain ε_y（10^{-6}）	Modulus of elasticity E_S（N/mm²）
Stainless steel bar	6	506.0	770.2	2405	203240
	16	513.2	766.9	2530	204340
	20	527.1	780.6	2477	203029
HRB400E steel bar	6	474.2	562.6	2258	210000
	16	436.7	616.0	2183	200000
	20	450.5	613.4	2253	200000

Table 7. Main parameters of finite element model

Model number	BJD-1	BJD-1-01	BJD-1-02	BJD-1-03	BJD-1-04	BJD-1-05	BJD-1-06
Strength grade of concrete	C40	C40	C40	C40	C40	C40	C40
hoop ratio of joint core area (%)	0.57	0.57	0.57	0.57	0.57	——	1.13
Longitudinal reinforcement ratio of column (%)	1.51	1.51	1.51	0.64	2.01	1.51	1.51
Axial compression ratio	0.3	0.05	0.6	0.3	0.3	0.3	0.3

——：The core area of the joint is not provided with stirrup.

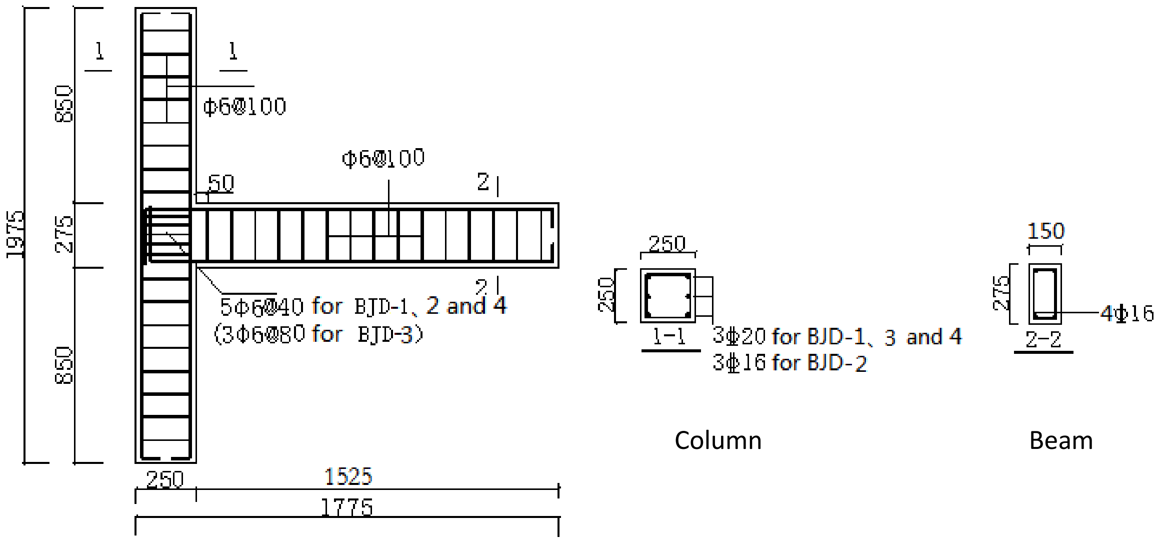

(a) Elevation (b) Cross-section

Fig. 1. Details of Tested Joints.

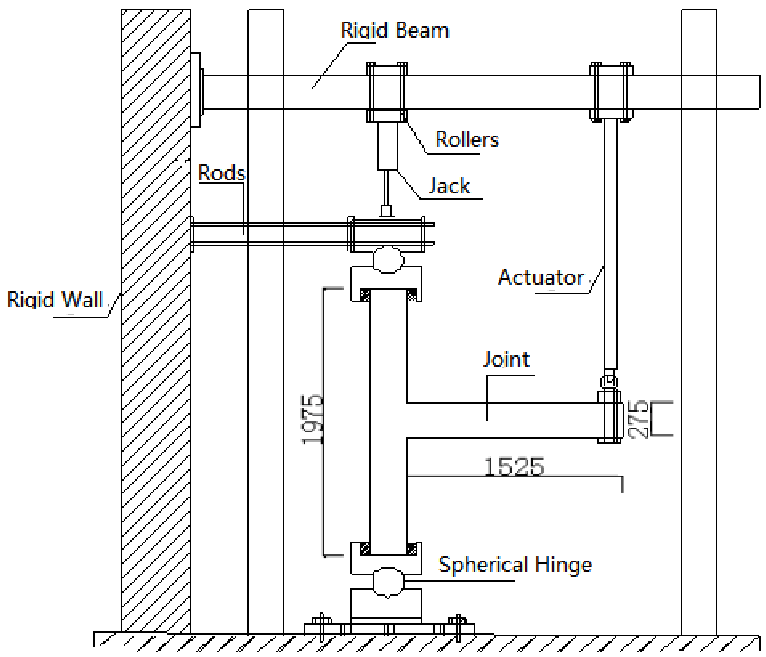

Fig. 2. Test equipment and layout.

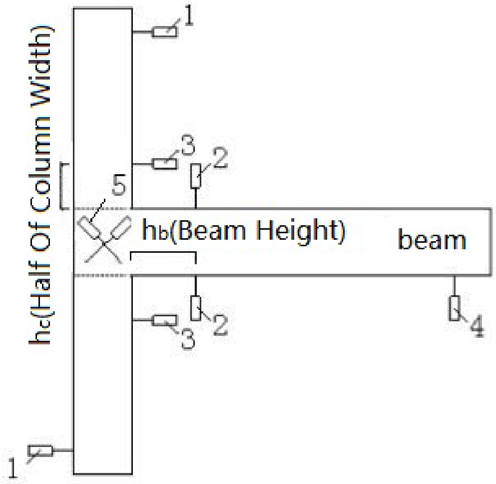

Fig. 3. LVDT placement and layout.

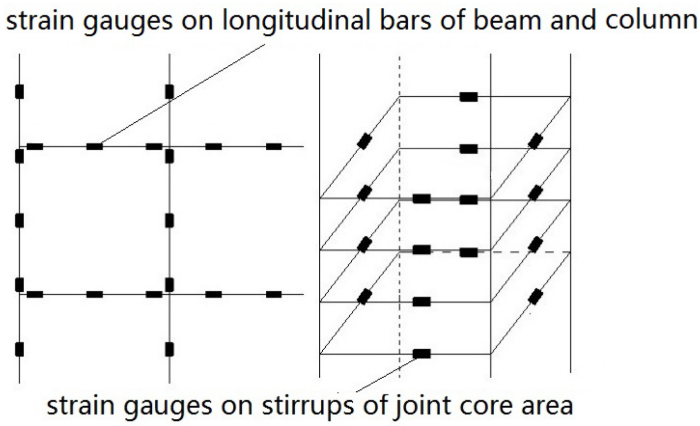

Fig. 4. Test strain gauge and layout.

(a) First observed crack in the beam

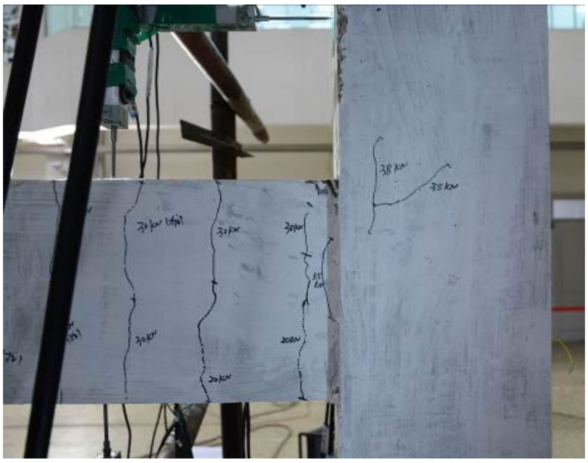

(b) First observed diagonal crack in the joint

(c) Formation of a full-height crack in the beam

(d) The joint at failure

Fig. 5. Process of damage in BJD-1.

Fig. 6. Damage in BJD-2.

Fig. 7. Damage in BJD-3.

Fig. 8. Damage in BJD-4.

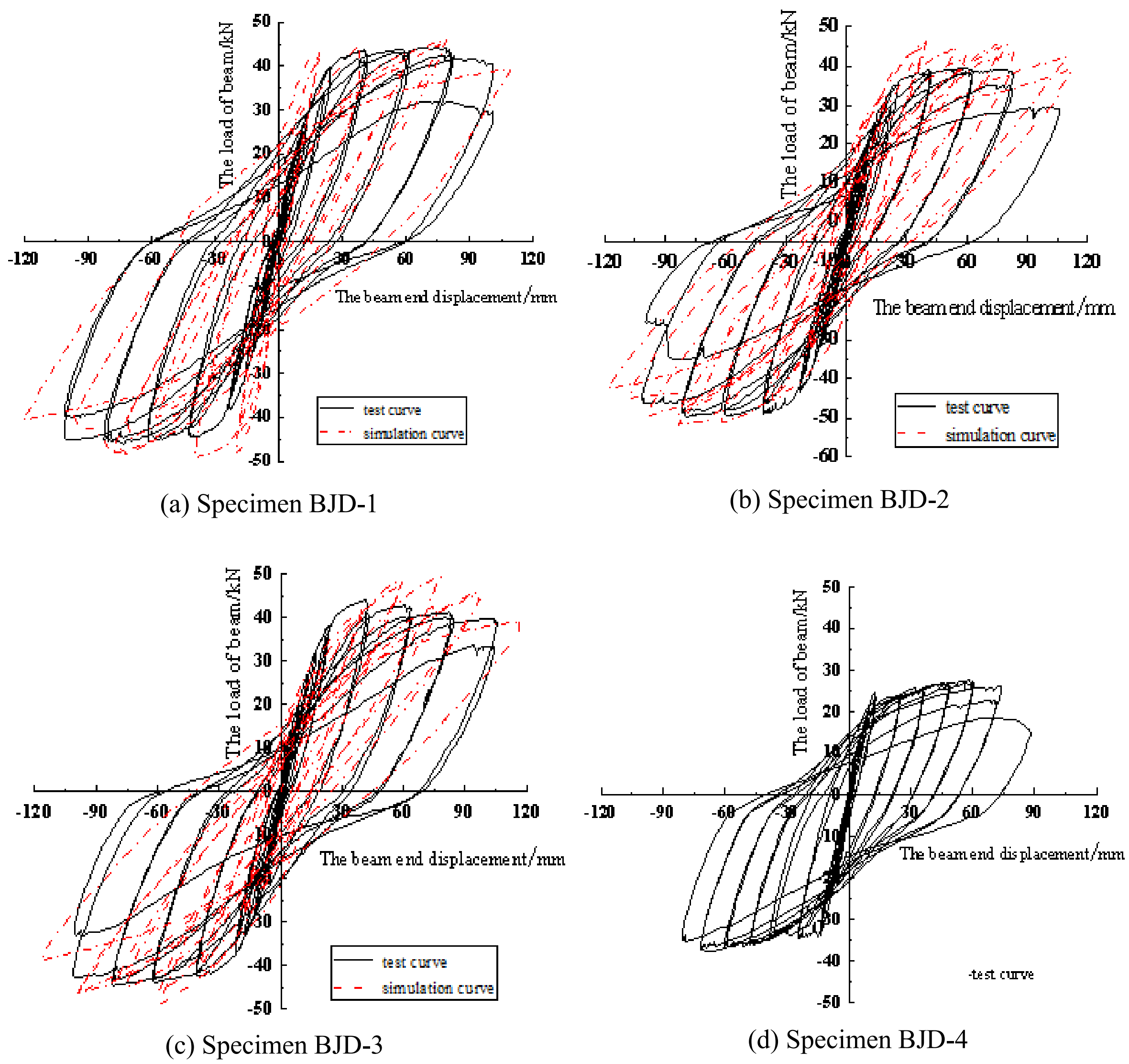

(a) Specimen BJD-1

(b) Specimen BJD-2

(c) Specimen BJD-3

(d) Specimen BJD-4

Fig. 9. Hysteresis curve for different specimens.

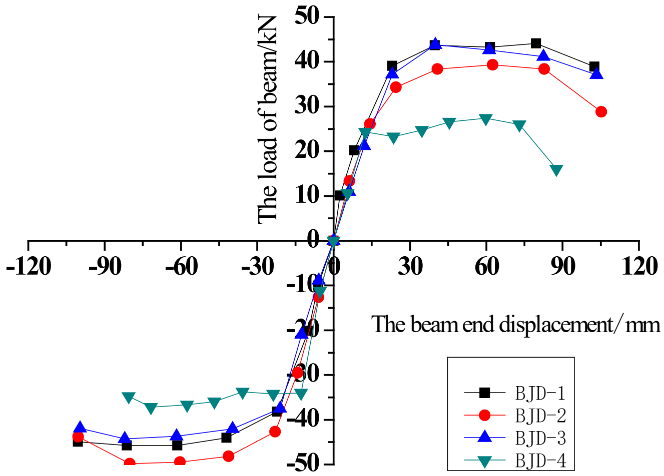

Fig. 10. Skeleton curve.

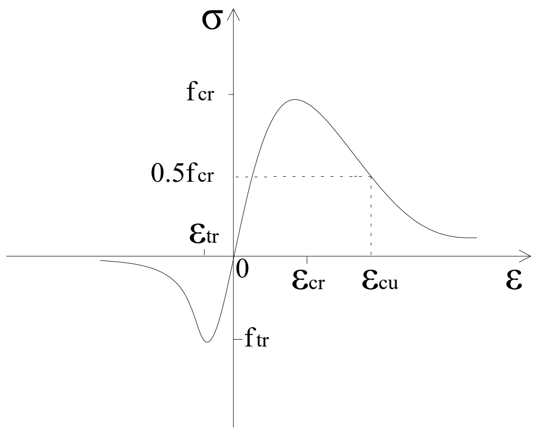

Fig. 11. Concrete stress - strain curve.

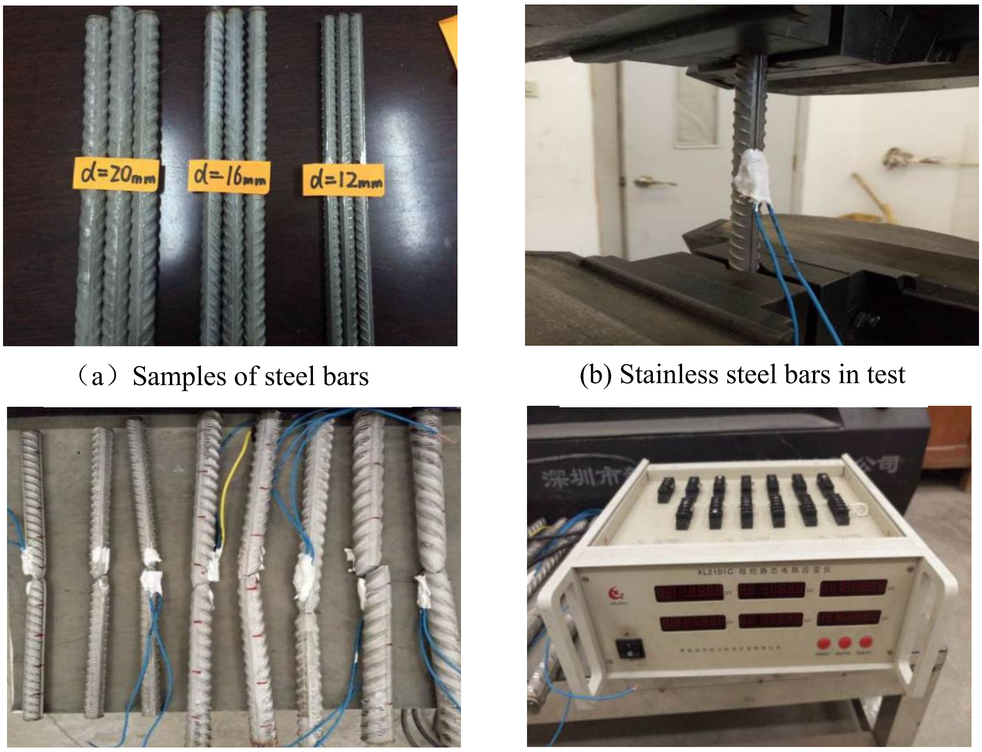

（a） Samples of steel bars

(b) Stainless steel bars in test

(c) Stainless steel bar after tension

(d) Strain collector

Fig. 12. Steel rebal mechanical property testing.

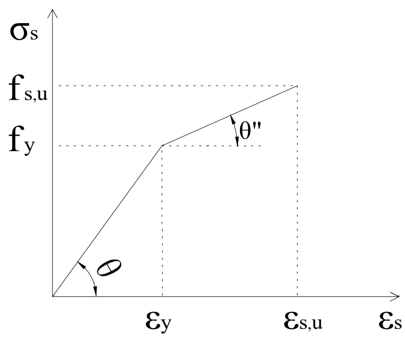

Fig. 13. Mathematical model of stress-strain curve of steel bar.

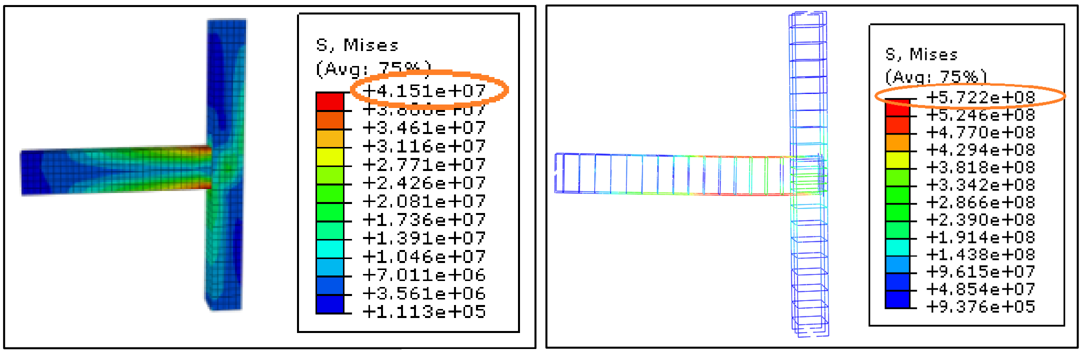

(a) Specimen BJD-1

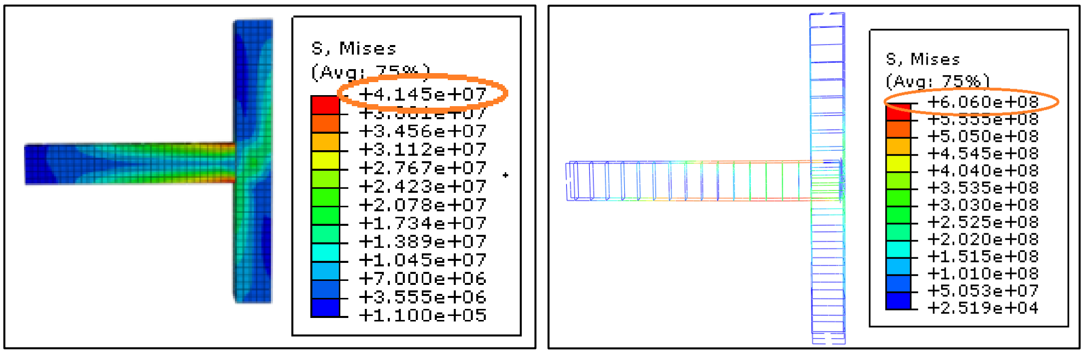

(b) Specimen BJD-2

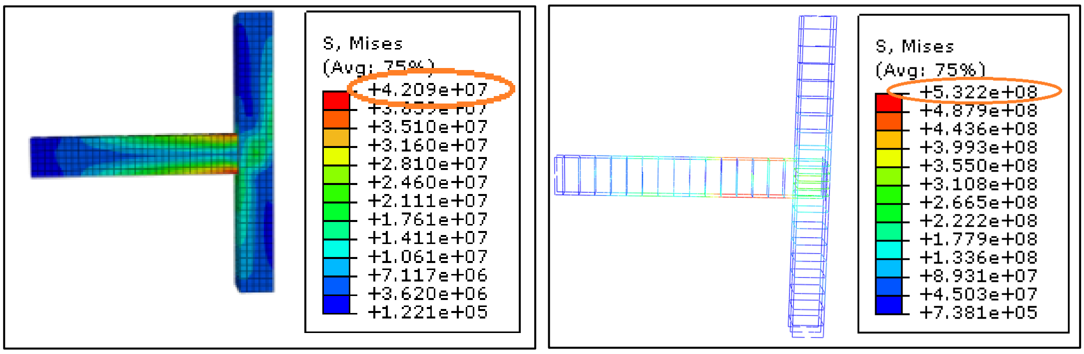

(c) Specimen BJD-3

Fig. 14. Simulation failure modes.

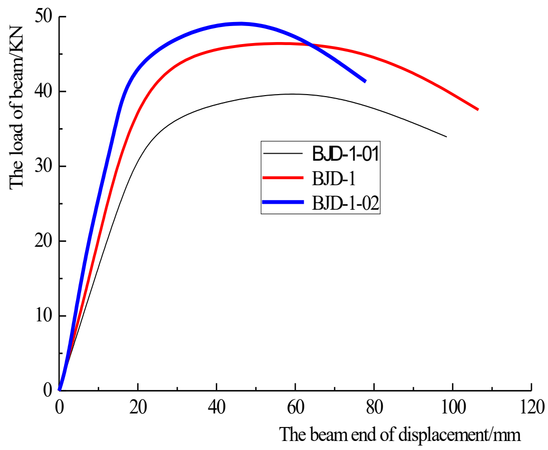

Fig. 15. Influence of axial compression ratio.

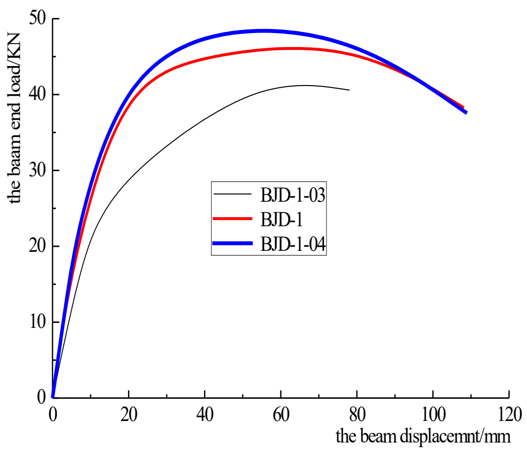

Fig. 16. Influence of column reinforcement ratio.

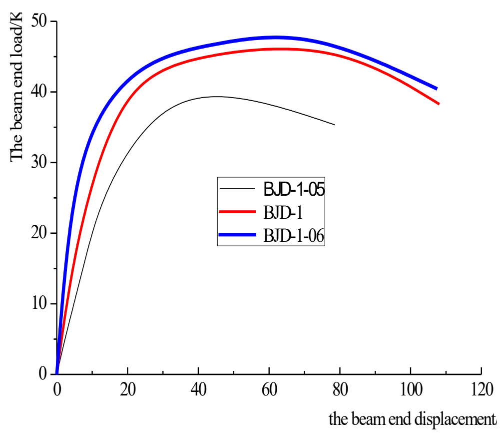

Fig . 17. Analysis of hoop ratio in joint core area.